

X-ray back-diffraction: can we further increase the energy resolution by tuning the energy slightly below that of exact backscattering?

M. G. Honnicke, N. Bouet

To be published in "JOURNAL OF APPLIED CRYSTALLOGRAPHY"

December 2019

Photon Sciences

Brookhaven National Laboratory

U.S. Department of Energy

USDOE Office of Science (SC), Basic Energy Sciences (BES) (SC-22)

Notice: This manuscript has been authored by employees of Brookhaven Science Associates, LLC under Contract No. DE-SC0012704 with the U.S. Department of Energy. The publisher by accepting the manuscript for publication acknowledges that the United States Government retains a non-exclusive, paid-up, irrevocable, world-wide license to publish or reproduce the published form of this manuscript, or allow others to do so, for United States Government purposes.

DISCLAIMER

This report was prepared as an account of work sponsored by an agency of the United States Government. Neither the United States Government nor any agency thereof, nor any of their employees, nor any of their contractors, subcontractors, or their employees, makes any warranty, express or implied, or assumes any legal liability or responsibility for the accuracy, completeness, or any third party's use or the results of such use of any information, apparatus, product, or process disclosed, or represents that its use would not infringe privately owned rights. Reference herein to any specific commercial product, process, or service by trade name, trademark, manufacturer, or otherwise, does not necessarily constitute or imply its endorsement, recommendation, or favoring by the United States Government or any agency thereof or its contractors or subcontractors. The views and opinions of authors expressed herein do not necessarily state or reflect those of the United States Government or any agency thereof.

X-ray back-diffraction: can we further increase the energy resolution by tuning the energy slightly below that of exact backscattering?

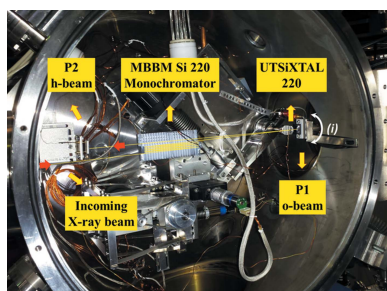
Marcelo Goncalves Hönnicke,^{a*} Cesar Cusatis,^b Raymond Conley,^c Edson Massayuki Kakuno,^d Elina Kasman,^c XianRong Huang,^c Nathalie Bouet,^e Juan Zhou,^e Yong Q. Cai,^e Joao Basso Marques^f and Flavio Cesar Vicentin^g

^aInstituto de Ciencias da Vida e da Natureza, Universidade Federal da Integracao Latino-Americana, 2044, Foz do Iguacu, Parana 85867-970, Brazil, ^bDepartamento de Fisica, Universidade Federal do Parana, 19091, Curitiba, Parana 81531-980, Brazil, ^cAdvanced Photon Source, Argonne National Laboratory, 9700 South Cass Avenue, Argonne, Illinois 60439, USA, ^dUniversidade Federal do Pampa, Travessa 45, 165, Bage, Rio Grande do Sul 96413-170, Brazil, ^ePhoton Sciences, Brookhaven National Laboratory, Upton, NY 11973, USA, ^fInstituto de Fisica, Universidade Federal do Mato Grosso, Avenida Fernando Correa da Costa, 2367, Cuiaba, Mato Grosso 78060-900, Brazil, and ^gLaboratorio Nacional de Luz Sincrotron (LNLS), Centro Nacional de Pesquisa em Energia e Materiais (CNPEM), Campinas, Sao Paulo 13083-970, Brazil. *Correspondence e-mail: marcelo.honnicke@unila.edu.br

X-ray beams at energies tuned slightly below that of exact backscattering (extreme conditions, where X-ray back-diffraction is almost extinguished – called residual XBD) are better focused if the experiment is carried out at lower energies in order to avoid multiple-beam diffraction effects. Following previous work by the authors [Hönnicke, Conley, Cusatis, Kakuno, Zhou, Bouet, Marques & Vicentin (2014). *J. Appl. Cryst.* **47**, 1658–1665], herein efforts are directed towards characterizing the residual XBD beam of an ultra-thin Si 220 crystal (UTSiXTAL) at ~ 3.2 keV. To achieve the residual XBD condition the UTSiXTAL was cooled from 310 to 273 K. The results indicate that under this extreme condition the energy resolution can be further improved. Issues with the energy resolution measurements due to incoming beam divergence and the ultra-thin crystal flatness are discussed.

1. Introduction

High- to ultra-high-energy-resolution X-ray experiments require the use of X-ray back-diffraction (XBD) geometry (Sykora & Peisl, 1970; Kohra & Matsushita, 1972; Brümmer *et al.*, 1979; Caticha & Caticha-Ellis, 1982; Graeff & Materlik, 1982; Aleksandrov *et al.*, 1984). Back-diffraction geometry has previously been studied with neutrons, this work being motivated by Heinz Maier-Leibnitz and carried out by Alefeld (1966). Various XBD optics instruments, particularly monochromators and analysers, have been proposed and implemented (Schülke & Nagasawa, 1984; Chang *et al.*, 2005; Shvyd'ko *et al.*, 2003, 2006; Huang, 2011; Huang *et al.*, 2012; Kim *et al.*, 2018) in order to optimize the photon flux/energy resolution in such experiments. Currently, the major application of XBD instrumentation is for inelastic X-ray scattering experiments (Cai, 2004; Tirao *et al.*, 2004; Fister *et al.*, 2006; Hill *et al.*, 2007; Verbeni *et al.*, 2009; Sergueev *et al.*, 2011; Cai *et al.*, 2013; Mortensen *et al.*, 2013; Sokaras *et al.*, 2013; Ishikawa *et al.*, 2015; Bolmatov *et al.*, 2017). X-ray imaging techniques using XBD have also been proposed (Hönnicke *et al.*, 2008; Hönnicke & Cusatis, 2009), and special attention has been given to the chemical bond contrast imaging techniques (Huotari *et al.*, 2011; Sahle *et al.*, 2017), since these may find use in a variety of applications.



The fundamental XBD properties can be studied in a simpler way at lower X-ray energies, where the diffraction profiles can be calculated by using only the two-beam case (two reciprocal lattice points close to the Ewald sphere) since multiple-beam diffraction (MBD) does not occur. Hashizume & Nakahata (1988) showed that mosaic Cu 111 crystals diffract X-rays like perfect crystals in the XBD geometry. Hönnicke *et al.* (2014) carried out low-energy XBD on ultra-thin Si crystals (5 μm thick) by measuring the forward o -beam profile using the Si 220 reflection including non-spurious measurements (*i.e.* with the absence of MBD) at the XBD condition where the energy is tuned slightly below that of exact backscattering.

Following our previous experiment (Hönnicke *et al.*, 2014), in the present work we attempt to characterize the back-diffracted h -beam from the ultra-thin Si crystal (220 reflection and 5 μm thick) (UTSiXTAL) at the XBD condition where the energy is tuned slightly below that of exact backscattering (here called the residual XBD). The UTSiXTAL is used again because it allows us to monitor the XBD conditions while characterizing the diffracted h -beam. Our goal is to determine whether the energy resolution under such extreme conditions can be further improved in comparison with that for the exact XBD condition. For this purpose, the XBD h -beam is characterized by using a grade A high-quality α -SiO₂ 11 $\bar{2}$ 0 single crystal (TEW, Japan) (Sutter *et al.*, 2006; Hönnicke *et al.*, 2013, 2016; Ketenoglu *et al.*, 2015; Yavaş *et al.*, 2017; Gog *et al.*, 2018; Kim *et al.*, 2018; Huang *et al.*, 2018; Said *et al.*, 2018, Macrander *et al.*, 2019) as the analyser at energies around 3.2 keV.

2. Concurrent measurement of the forward o -beam back-diffraction and the back-diffracted h -beam

As the first step in characterization, in terms of energy resolution, of the back-diffracted h -beam of the UTSiXTAL, we improved our previous experimental setup (Hönnicke *et al.*, 2014) in order to detect, simultaneously, both the forward back-diffracted o -beam and the back-diffracted h -beam. We have adopted this methodology for several different reasons: (i) to reinforce the angular tilt adjustment of the UTSiXTAL so that it can be oriented to produce accurate XBD conditions; (ii) to achieve, at room temperature, the diffraction conditions that are as close as possible to the exact or

residual XBD condition; (iii) to optimize the analyser crystal (AC) angular position; and (iv) to monitor the UTSiXTAL XBD through the forward back-diffracted o -beam when the AC is in place. Similarly to our previous work (Hönnicke *et al.*, 2014), the experiment was carried out at the Soft X-ray Spectroscopy (SXS) beamline at Laboratório Nacional de Luz Síncrotron (LNLS, Brazil) (Fig. 1). An Ni-coated Si toroidal mirror is used to focus (6.7 mrad) the incident beam at the UTSiXTAL position, followed by an InSb 111 double-crystal monochromator (DCM) set at ~ 3.2 keV. Further downstream, in a ~ 40 cm diameter vacuum chamber (1×10^{-5} mbar = 1 mPa), an Si 220 channel-cut multi-bounce back-diffraction monochromator (MBBM) was used to increase the energy resolution $\Delta\lambda/\lambda \simeq 7 \times 10^{-5}$ at 3.2 keV. The estimated bandwidth ($\Delta\lambda/\lambda$) and divergence ($\Delta\theta_{\text{div}} \simeq 2.7 \times 10^{-4}$ rad) afforded by the MBBM is shown by the DuMond diagrams (DuMond, 1937) in Fig. 2. From inspection of the DuMond diagram in Fig. 2(a) it appears that, for exact back-diffraction, the energy resolution is infinitely small. However, the equations that appear in Fig. 2(c) imply an energy resolution limit for exact XBD which is based on the differentiation of the general form of Bragg's law for the symmetric Bragg case (Hönnicke *et al.*, 2013),

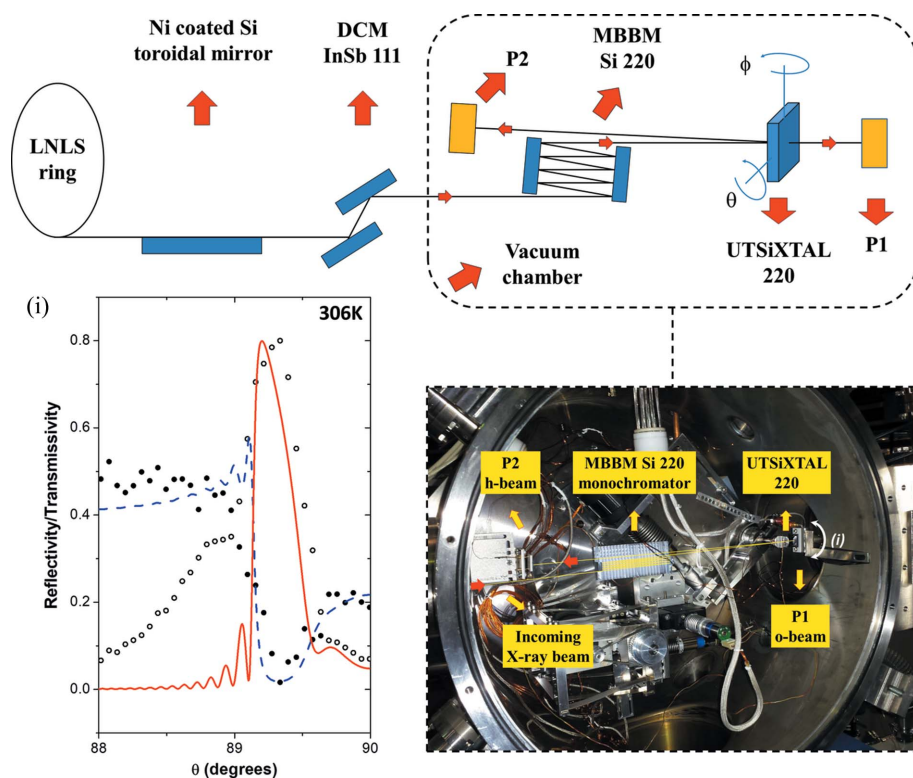


Figure 1

Experimental setup for the UTSiXTAL alignment detecting both the forward back-diffracted o -beam and the back-diffracted h -beam simultaneously. The inset (bottom right) shows details of the experimental setup inside the vacuum chamber. The graph labelled (i) shows the measured XBD profiles of the θ scan (open circles – diffracted h -beam detected by P2; closed circles – forward diffracted o -beam detected by P1) and theoretically simulated XBD profiles based on the extended dynamical theory of X-ray diffraction for perfect crystals (solid red line – diffracted h -beam; dashed blue line – forward diffracted o -beam) under the condition of eight bounces in the MBBM.

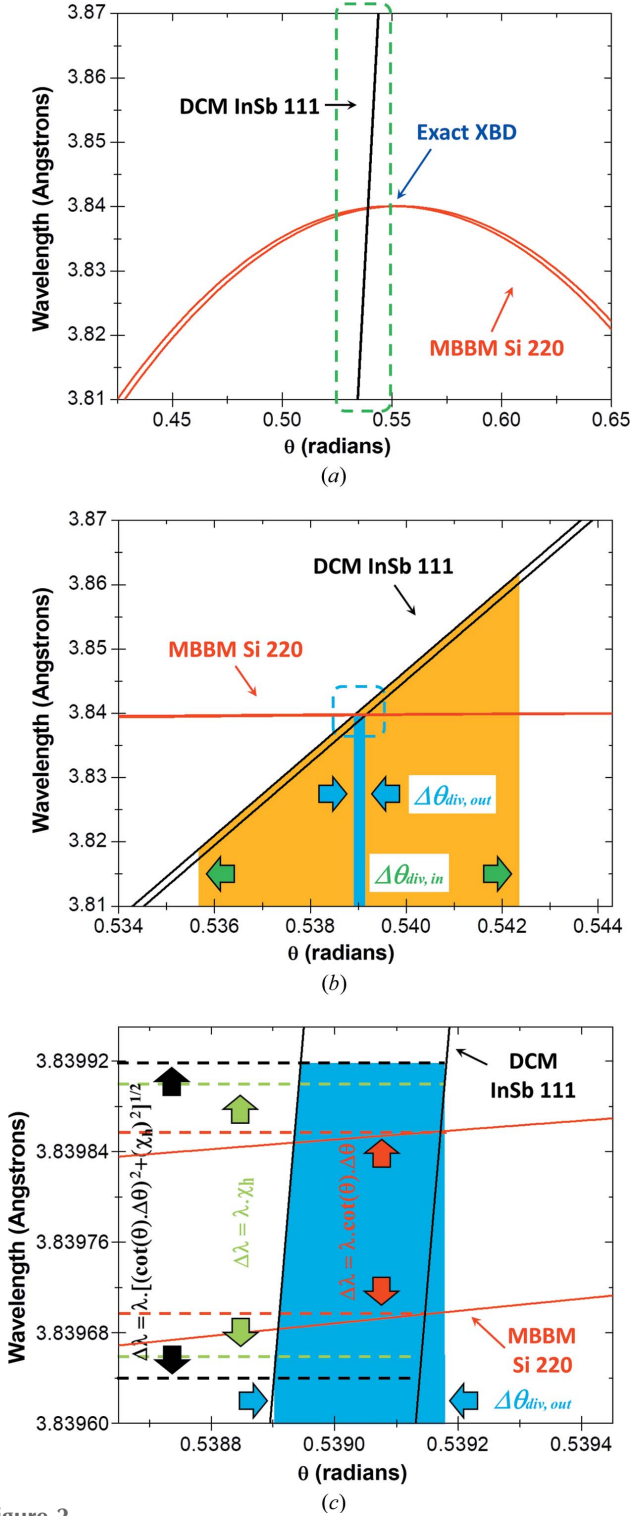


Figure 2

DuMond diagrams (DuMond, 1937) used to estimate the divergence and bandwidth obtained with the Si 220 MBBM. (a) DuMond diagram overview for the InSb 111 DCM and the MBBM showing the region of exact XBD where the energy resolution ($\Delta\lambda/\lambda$) appears infinitely small. (b) Enlargement of the area indicated by dashed green lines in (a), where the incoming divergence (provided by the focusing toroidal mirror) and outgoing divergence are exposed. (c) Enlargement of the area indicated by dashed blue lines in (b). Since the MBBM is a perfect crystal and is close to XBD, its $\Delta\lambda/\lambda$ is given by equation (1), with the contribution of only two terms, since $\Delta d/d$ is too small. Even considering only these two terms, $\Delta\lambda/\lambda$ is close to the XBD limit, i.e. $|\chi_h|$.

$$\left(\frac{\Delta\lambda}{\lambda}\right)^2 = \left(\frac{\Delta E}{E}\right)^2 = \left(\frac{\Delta d}{d}\right)^2 + [\cot g(\theta)\Delta\theta_{\text{div}}]^2 + (-C|\chi_h|)^2, \quad (1)$$

where θ is the diffraction angle, $\Delta d/d$ is the relative variation in the lattice parameter and χ_h is the polarizability. If the crystal is perfect ($\Delta d/d \simeq 10^{-7}$ – 10^{-9}) and it is at back-diffraction ($\theta = \pi/2$) the energy resolution has a limit given by $|\chi_h|$. The MBBM can be adjusted to diffract X-rays within the InSb 111 DCM bandwidth, from six to ten bounces. The UTSiXTAL (Hönnicke *et al.*, 2014) was used as the XBD crystal. The beam footprint on the UTSiXTAL was $\sim 1 \times 2$ mm (V \times H). A 50 μm CVD diamond optical plate (Applied Diamond Inc.) was used as a support for the UTSiXTAL and was glued onto a Peltier cooler to allow temperature control. Measurements were taken from 310 K down to 273 K, which is adequate, for ten bounces in the MBBM, to go from the exact XBD condition to the residual XBD (where the back-diffraction is almost extinguished). In order to monitor changes in the incoming X-ray beam energy during the XBD measurements, another temperature sensor was also used to monitor the MBBM temperature, which was kept at 300 K. The XBD profiles were measured by rocking the UTSiXTAL [θ scan, (i) in Fig. 1] and detecting the diffracted intensities (forward back-diffracted *o*-beam and back-diffracted *h*-beam) by two PIN diodes in photocurrent mode (Fig. 1). The first PIN diode (P1) was set just downstream of the UTSiXTAL (for the forward *o*-beam XBD measurement). The second PIN diode (P2) (for the *h*-beam XBD measurement) was set ~ 40 cm upstream, with its center ~ 4 mm above the incoming X-ray beam on the UTSiXTAL (around 14 mm above the incoming X-ray beam in the vacuum chamber), forming a diffraction angle of around 89.7° with the center of the *h*-beam XBD profile.

During the experiment, the UTSiXTAL was firstly rotated (ϕ angle, in Fig. 1) to find the maximum angular distance between the two forward *o*-beam XBD profiles in θ scans taken at each ϕ angle. Since the vacuum chamber was previously aligned, once the maximum angular distance between the two forward back-diffracted *o*-beam profiles is achieved, detection of the back-diffracted *h*-beam is straightforward in the second PIN diode (P2) located 40 cm upstream. A typical XBD measurement of the simultaneous *o*-beam and *h*-beam in the θ scan at 306 K with eight bounces in the MBBM is shown in the graph of Fig. 1(i).

3. Setting up the $\alpha\text{-SiO}_2$ $11\bar{2}0$ analyser crystal

An $\alpha\text{-SiO}_2$ $11\bar{2}0$ AC (Fig. 3) was oriented and cut by a dicing saw with a metal-bonded diamond blade into a slab with dimensions of $33 \times 38 \times 3$ mm from a grade A $\alpha\text{-SiO}_2$ single-crystal block (TEW Japan). Grade B (Sutter *et al.*, 2005) and grade A (Sutter *et al.*, 2006; Hönnicke *et al.*, 2013; Ketenoglu *et al.*, 2015; Huang *et al.*, 2018; Macrander *et al.*, 2019) $\alpha\text{-SiO}_2$ single crystals (TEW Japan) have been previously characterized and it was found that the relative variations in the lattice parameters ($\Delta d/d$) are smaller than 1×10^{-7} for the grade A

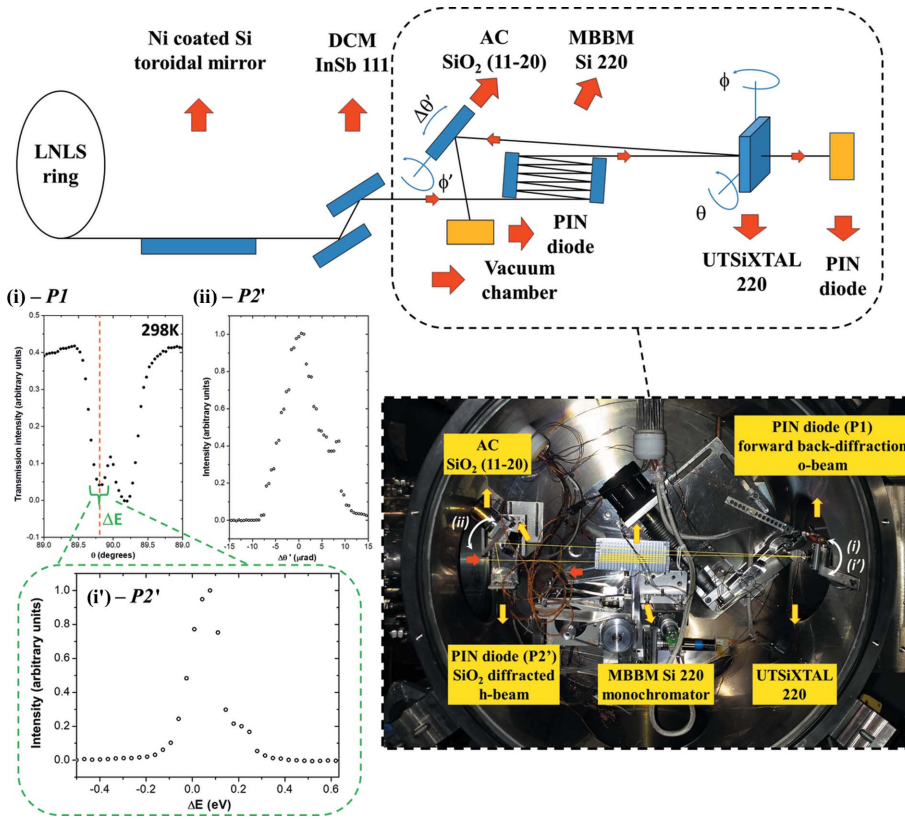


Figure 3

Schematic representation of the experimental setup for analysing the UTSiXTAL back-diffracted h -beam as a function of temperature with the α -SiO₂ 11 $\bar{2}$ 0 AC. The bottom right inset shows all the optical elements of the experimental setup inside the vacuum chamber. (i) θ scan for acquisition of the forward XBD o -beam profiles, detected with the first PIN diode (P1). (i') ΔE (θ scan) for determining the energy resolution, detected with the second PIN diode (P2'). (ii) $\Delta\theta'$ scan for the AC diffraction optimization (by adjusting the tilt angle ϕ') also detected with the second PIN diode (P2'). Ten bounces in the MBBM.

quartz, *i.e.* this quartz single crystal can be considered to be a perfect crystal. This conclusion has been confirmed by the use of grade A quartz in high- to ultra-high-resolution inelastic X-ray scattering experiments (Ketenoglu *et al.*, 2015; Honnicke *et al.*, 2016; Yavaş *et al.*, 2017; Gog *et al.*, 2018; Kim *et al.*, 2018; Said *et al.*, 2018). In the current experiment, the larger side (38 mm) of the quartz crystal was made with a strain-relief cut in order to fix the crystal slab in a clamp support by preventing the propagation of strains in the crystal diffraction volume. Subsequently, the AC was lapped (SiC abrasive, grit 800) and etched in HF (48%) for 2 h at 298 K.

With the UTSiXTAL in place and aligned to maximize the back-diffracted h -beam at the second PIN diode position (P2), we proceeded to mount the AC (Fig. 3). The AC was fixed in a goniometric piezo cradle for angular scans [$\Delta\theta'$ scan, see (ii) in Fig. 3] and tilt adjustment (ϕ'). The AC was centered at the previous second PIN diode position (P2 in Fig. 1) and the UTSiXTAL was set at the XBD condition [Fig. 3(i)] at a fixed θ angle [$\sim 89.7^\circ$; red dashed line in Fig. 3(i)]. For detecting the AC diffraction, the second PIN diode was set at the bottom position in the vacuum chamber (P2' in Fig. 3). The diffraction condition of the AC was then found with a $\Delta\theta'$ angular scan [Fig. 3(ii)]. The diffraction conditions were optimized on the

basis of the AC angular diffraction profile width, which is maximized by changing the tilt angle (ϕ') in several different $\Delta\theta'$ angular scans. Then, for each different temperature on the UTSiXTAL (at a fixed angle of 89.7°), an AC angular scan [$\Delta\theta'$, Fig. 3(ii)] was made to set the AC at the maximum intensity. Afterwards, an energy scan [Fig. 3(i')], for each different temperature was carried out by another θ scan on the UTSiXTAL. The effect of scanning on different areas of the AC surface (arc arrow effect) is negligible since the θ scan is on the order of just a few tenths of a degree.

4. Forward o -beam back-diffraction and energy resolution measurements

With all the optical elements aligned and optimized, we started the energy resolution measurements. As mentioned above, under the condition of ten bounces in the MBBM, at each different temperature of the UTSiXTAL from 310 K down to 273 K, the following sequence of measurements/procedures was applied in order to perform an energy resolution scan: (i) a forward back-diffracted o -beam profile (θ scan) was acquired [Fig. 4(a)] (to go from the exact XBD condition

and further); (ii) the UTSiXTAL was set at $\sim 89.7^\circ$ [red dashed line in Fig. 4(a)]; (iii) the α -SiO₂ 11 $\bar{2}$ 0 was set at its diffraction condition (the angular position where the intensity is at its maximum); and (iv) the energy resolution scan was performed by rocking the UTSiXTAL again (θ scan). The energy resolution scans at each different temperature of the UTSiXTAL are shown in Fig. 4(b). To convert the θ scan to energy units (eV), a rule of three was employed:

$$\chi_h \rightarrow \Delta\theta_{310\text{K}}, \quad \Delta E/E \rightarrow \Delta\theta_T, \quad (2)$$

where $\Delta E/E$ is the relative energy resolution, $\Delta\theta_T$ is the angular width of the θ scan measured by the second PIN diode (P2') for the UTSiXTAL at each different temperature T (from 310 down to 273 K), $\Delta\theta_{310\text{K}}$ is the angular width of the θ scan measured by P2' for the UTSiXTAL at 310 K (which approximately corresponds to the exact XBD condition) and χ_h is the polarizability that gives the energy resolution at the exact XBD condition. Therefore, the following equation is applied,

$$\frac{\Delta E}{E} = \Delta\theta_T \frac{\chi_h}{\Delta\theta_{310\text{K}}}. \quad (3)$$

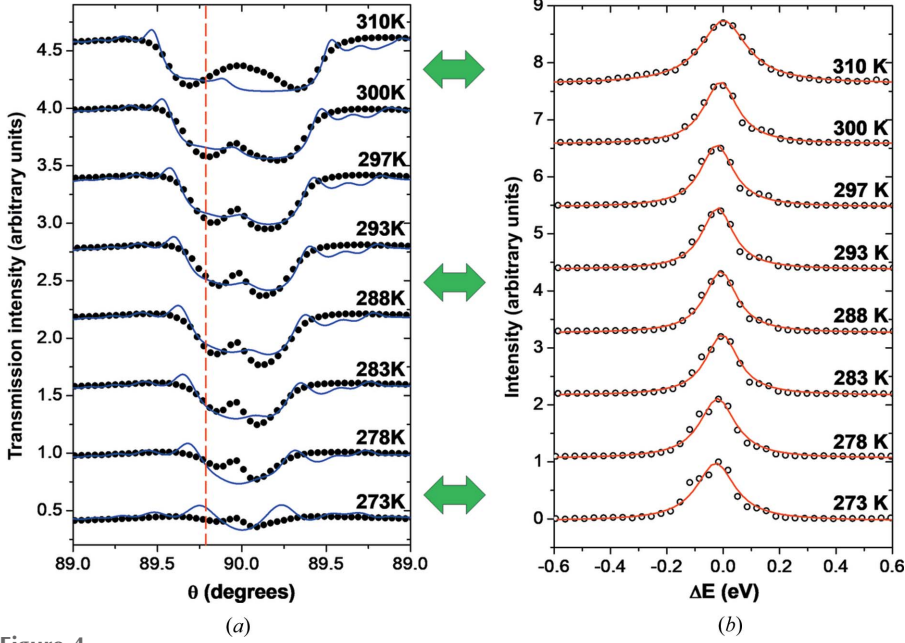


Figure 4

(a) Forward o -beam XBD profiles at different temperatures with ten bounces in the MBBM. A temperature of 310 K approximately corresponds to the UTSiXTAL exact XBD condition. For each different temperature of the UTSiXTAL, a θ scan around $\sim 89.7^\circ$ (red dashed line) is carried out with the α -SiO₂ 11 $\bar{2}0$ AC set at the angular position where the diffraction has maximum intensity. The intensity as a function of the angle is registered by the second PIN diode (P2', see Fig. 3). Then, following equation (3) the scans are converted into energy units (b) in order to perform the energy resolution measurements at each different temperature of the UTSiXTAL.

Then each scan in Fig. 4(b) was fitted by a Lorentzian profile. The fitted full width at half-maximum can be considered as the measured energy resolution at each temperature. The fitting results are shown in Fig. 5, which indicates that the energy resolution of the XBD can indeed be increased (*i.e.* has the smallest value) in the residual back-diffraction region (corresponding to the diffraction condition where the energy is tuned slightly below that of exact backscattering), *i.e.* between 290 and 295 K. However, if the temperature is further reduced, *i.e.* corresponding to the diffraction conditions where the energies are tuned even further below that of exact backscattering, the energy resolution appears to increase again. To estimate the energy resolution in the residual XBD region, we fit a polynomial function to the energy resolution results. The best fit, *i.e.* the fitting with the smallest standard deviation value, was found with a fourth-order polynomial.

Since we did not directly measure the bandwidth, a discussion on the beam divergences throughout the setup is convenient. As stated in Section 2, from the DuMond diagrams (DuMond, 1937) shown in Fig. 2, we could estimate the outgoing MBBM bandwidth ($\Delta\lambda/\lambda \simeq 7 \times 10^{-5}$) and divergence ($\Delta\theta_{\text{div}} \simeq 2.7 \times 10^{-4}$ rad). These numbers were used to build a new set of DuMond diagrams (Fig. 6) for the MBBM/UTSiXTAL and UTSiXTAL/AC in order to discuss the sensitivity/validity of the presented energy resolution results. The outgoing MBBM $\Delta\lambda/\lambda$ and $\Delta\theta_{\text{div}}$ are restricted by the DCM and the MBBM itself. Since the UTSiXTAL back-diffraction h -beam profile covers a much wider angular

range than the divergence, at each allowed diffraction energy (bandwidth) within the UTSiXTAL back-diffraction h -beam profile, each $\Delta\theta_{\text{div}}$, in principle, has the same value as the MBBM outgoing $\Delta\theta_{\text{div}}$ [Fig. 6 (a)]. Hence, what we termed the energy scan is only the MBBM $\Delta\theta_{\text{div}}$ scan across the AC, and since the AC diffraction h -beam profile width does not change by more than a few μrad between the different employed energies, the results shown in Fig. 5 should appear constant, since all $\Delta\theta_{7\text{s}}$ (including $T = 310$ K) would be equal to $\Delta\theta_{\text{div}}$. However, this was not observed and the results can still be attributed to the energy resolution changes. One reason could be that the energy resolution of the UTSiXTAL at exact XBD [Fig. 6(a)] is slightly smaller than the MBBM $\Delta\lambda/\lambda$ and could be even smaller in the residual XBD condition. Another possible cause could be the almost non-dispersive setup of the MBBM and UTSiXTAL (remembering that, even for the same temperature, their XBD profiles are different since they are prepared from different ingots). In this case, we should

have an overlap between the two h -beam back-diffraction profiles [Fig. 6(b)] which could diminish the outgoing divergence (if the profile flanks overlap) or increase the outgoing divergence (if the profile tails overlap) for the UTSiXTAL residual XBD condition. These two assumptions could be used in an attempt to simulate the profiles measured and shown in Fig. 4(b). However, this can be achieved only for the exact UTSiXTAL XBD, where the h -beam back-diffraction profile

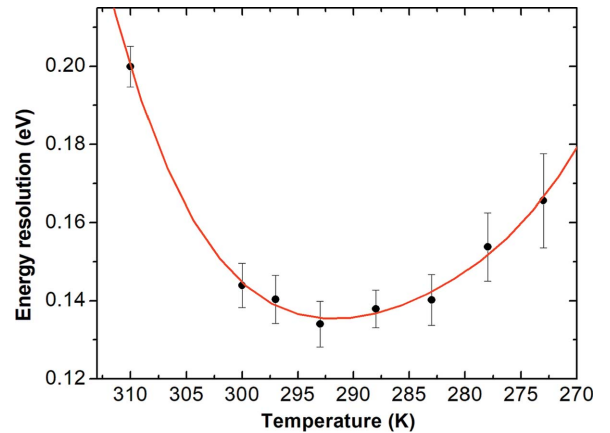


Figure 5

Energy resolution as a function of temperature. The results were extracted from Lorentzian fitting of the curves shown in Fig. 4(b). The solid red line shows a tentative fitting (fourth-order polynomial) in order to estimate the energy resolution in the residual XBD region.

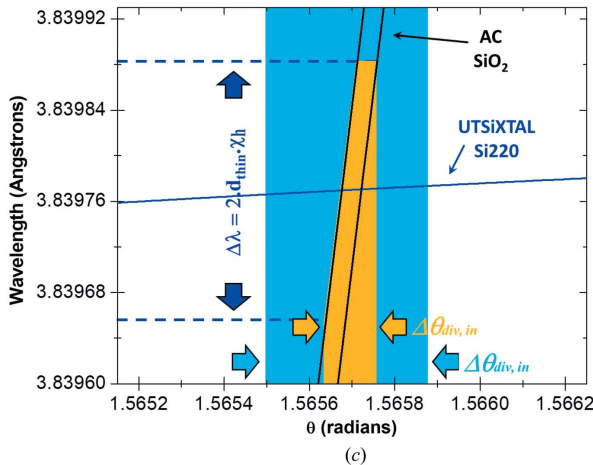
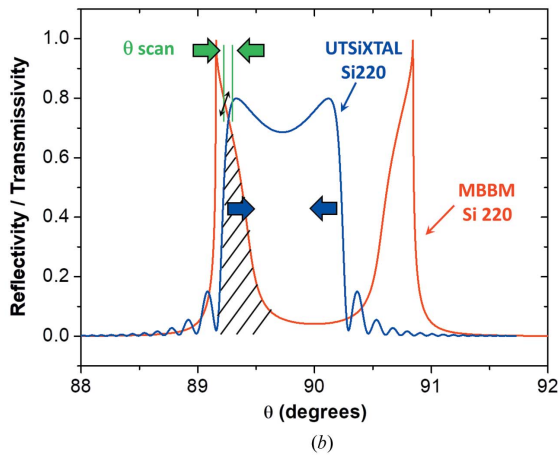
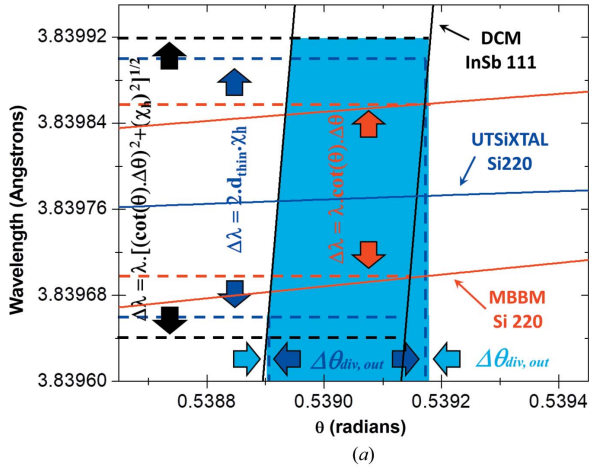


Figure 6

(a) DuMond diagram (DuMond, 1937) of the different optical elements aligned: InSb 111 DCM, Si 220 MBBM and the UTSiXTAL. Since the UTSiXTAL is at the exact back-diffraction (tilted by $\sim 0.3^\circ$) its energy resolution is higher than the MBBM and its corresponding $\Delta\theta_{div}$ is lower than the MBBM divergence. (b) MBBM and UTSiXTAL (at exact XBD) XBD h -beam profiles overlapping (hatched area). The θ scan is very narrow considering the overlapping at this position. At the residual XBD conditions, the UTSiXTAL profile narrows, as indicated by the blue arrows. (c) DuMond diagram for the UTSiXTAL and the α -SiO₂ 11 $\bar{2}$ 0 AC. The outgoing divergence of the MBBM is also indicated. The expected resulting curve for the UTSiXTAL scan would be a convolution of a square-shaped divergence curve (modulated by the UTSiXTAL XBD h -beam profile) with the AC h -beam diffraction profile.

can be simulated. Even in that case, if we use DuMond-diagram type simulations, we have to specify the exact XBD profile width, since it appears as zero in the DuMond diagram. By inspection of the DuMond diagram in Fig. 6(c) it is possible to see that such a simulation would consist of a convolution of an almost square-shaped $\Delta\theta_{div}$ (since it is modulated by the UTSiXTAL back-diffraction h -beam profile) with the AC h -beam diffraction profile. For the residual XBD condition, the simulation of the h -beam back-diffraction profile becomes difficult as none of the diffraction angles play a role. This difficulty also appears in open-source software, such as *XOP* (Sanchez del Rio *et al.*, 2015). Hence, we do not have the exact parameters to include in the possible simulations. For better energy evaluation and to confirm the above assumption, a higher-energy-resolution DCM should be employed, *e.g.* an α -SiO₂ 11 $\bar{2}$ 0 monochromator.

Another point is that, in Fig. 4(a), the forward o -beam XBD profiles exhibit a bump, which differs from the measurements in our previous work (Hönnicke *et al.*, 2014). This bump was not expected because, as described in our previous work, even under the condition that the UTSiXTAL has strong stresses, the measured back-diffracted o -beam profiles should still be very close to the theoretical calculations (based on the extended dynamical theory of X-ray diffraction for perfect crystals). One reason for the presence of the bump could be the different misorientations on the UTSiXTAL at the glue points on the CVD diamond optical plate support, as schematically shown in Fig. 7(a). This indicates that, in our previous work, the beam footprint [1×2 mm (V \times H)] was fortunately far from the glue point. In the current experiment, since the crystal was set in a fixed stage so that it could not be translated easily across the beam, we tried to establish a very simple theoretical model to predict the experimental profiles in order to check if such a bump could affect our final results. From the surface metrology (profilometry), high-resolution rocking curve measurements and X-ray topography presented in our previous work (Hönnicke *et al.*, 2014), the UTSiXTAL misorientation can be quantified to have a maximum value of $\sim 0.41^\circ$. Thus, for calculating the forward XBD o -beam profile [solid blue lines in Fig. 4(a)], we consider the UTSiXTAL to consist of two different portions that diffract X-rays as two independent perfect crystals misoriented 0.41° apart. By successive approximations, we best fit the experimental results by assuming that one portion is covered by 80% of the beam footprint and another portion is covered by 20% [Fig. 7(b)]. With this model, we found that the simulation agrees well with the measurements; but there do exist some discrepancies between the theoretical and measured profiles, especially at 310, 283, 278 and 273 K. This can be attributed to thermal expansion of the multiple elements (Peltier, CVD diamond optical plate support, crystal support and even the UTSiXTAL), which changes the beam footprint position on the UTSiXTAL at the different specified temperatures. However, for energy resolution determination purposes, since the UTSiXTAL XBD h -beam comes from the low-angle side of the forward o -beam XBD profiles [dashed line in Fig. 4(a)], which is only slightly affected or unaffected by the diffraction

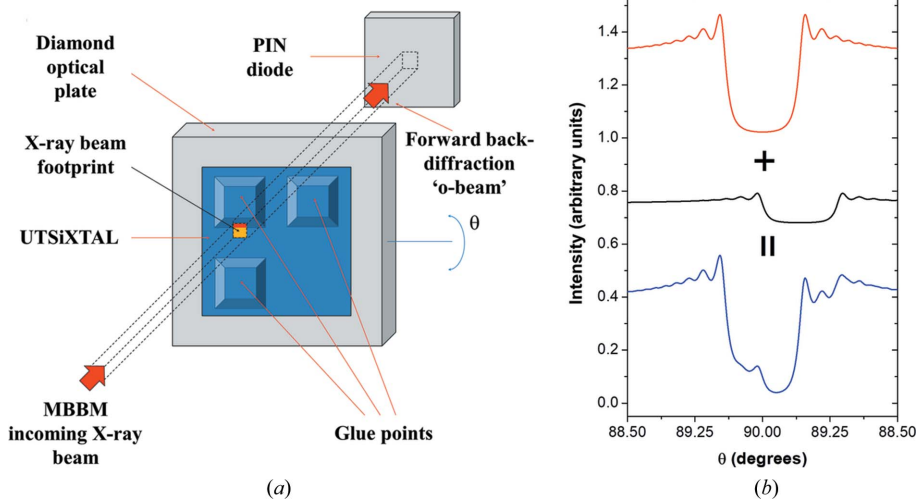


Figure 7

(a) Schematic representation of the misorientation (due to the glue points on the CVD diamond optical plate support) on the two different portions of the UTSiXTAL impinged by the X-ray beam. As 80% of the beam footprint is covering one portion and 20% is covering the other portion, it is possible to simulate the forward *o*-beam back-diffraction profile (b) by considering the two different UTSiXTAL portions diffracting as two independent perfect crystals set 0.41° apart (a previously known misorientation).

of the small misaligned crystal portion, we believe that the results shown in Fig. 4(b) are consistent with the diffraction of a perfect single crystal. However, an experiment with a flat crystal and using a higher-resolution DCM should be performed in order to check the validity of our results; this will be the subject of our future work.

5. Conclusions

We have characterized the back-diffracted *h*-beam corresponding to the condition where the energy is tuned slightly below that of exact backscattering (residual XBD). The XBD at lower energies (Si 220 at ~ 3.2 keV) was chosen in order to avoid multiple-beam diffraction effects. The residual XBD was achieved by keeping a $5\ \mu\text{m}$ -thick UTSiXTAL at a fixed angle while varying its temperature from 310 K (approximately the exact XBD condition) to 273 K. The energy resolution was determined by analysing the XBD *h*-beam with an $\alpha\text{-SiO}_2$ $11\bar{2}0$ AC. Our results suggest that the energy resolution can be increased in the residual XBD region. Note, if one looks carefully at the experimental setup, such results can be attributed to a divergence reduction. This was also attributed to the energy resolution increasing, partly due to the UTSiXTAL divergence and chromaticity coupling since the angular coverage of the XBD *h*-beam profile is much larger than the MBBM outgoing divergence. An unexpected bump in the forward transmitted XBD *o*-beam profiles was also detected, which is attributed to different misorientations of the UTSiXTAL due to the glue points on the CVD diamond optical plate support. In order to check if such a bump could affect the final results, we simulated the forward *o*-beam XBD profiles by considering two different UTSiXTAL portions that

diffract X-rays as two independent perfect crystals with an orientation difference of 0.41° (i.e. the previously measured misorientation; Hönnicke *et al.*, 2014). On the basis of this model, we found good agreement between the theoretical and measured profiles, except for a few discrepancies that we attributed to thermal expansion of the multiple elements (Peltier, CVD diamond optical plate support, crystal support and even the UTSiXTAL), causing beam footprint position changes on the UTSiXTAL at different temperatures. Since the UTSiXTAL XBD *h*-beam for the energy resolution determination comes from the low-angle forward *o*-beam XBD profile (which is only slightly affected or unaffected by the small misaligned portion diffraction) we believe that our energy resolution results should be the same for a perfect single crystal. An experiment with a better

energy resolution DCM (e.g. $\alpha\text{-SiO}_2$ $11\bar{2}0$) with a flat crystal will be performed in future in order to check the validity of our results.

Acknowledgements

The authors thank LNLS/CNPEN/MCT for beam time (proposal Nos. SXS-19050; SXS-Friendly User).

Funding information

The following funding is acknowledged: CNPq/PQ (scholarship Nos. 309109/2013-2; 309614/2013-9); US Department of Energy, Office of Science, Office of Basic Energy Sciences (contract No. E-AC02-06CH11357); US Department of Energy, Office of Science, Office of Basic Energy Sciences (contract No. DE-SC0012704).

References

- Alefeld, B. (1966). *Sitzungsber. Bayerischen Akad. Wiss.* p. 109.
- Aleksandrov, Yu. A., Chalupa, B., Kulda, J., Machekrina, T. A., Michalec, R., Mikula, P., Sedláková, L. N., Vávra, J. & Vrána, M. (1984). *Phys. Status Solidi A*, **83**, 455–460.
- Bolmatov, B., Zhernenkov, M., Sharpnack, L., Agra-Kooijman, D. M., Kumar, S., Suvorov, A., Pindak, R., Cai, Y. Q. & Cunsolo, A. (2017). *Nano Lett.* **17**, 3870–3876.
- Brümmer, O., Höche, H. R. & Nieber, J. (1979). *Phys. Status Solidi A*, **53**, 565–570.
- Cai, Y. Q. (2004). *AIP Conf. Proc.* **705**, 340–343.
- Cai, Y. Q., Coburn, D. S., Cunsolo, A., Keister, J. W., Honnicke, M. G., Huang, X. R., Kodituwakku, C. N., Stetsko, Y., Suvorov, A., Hiraoka, N., Tsuei, K. D. & Wille, H. C. (2013). *J. Phys. Conf. Ser.* **425**, 202001.
- Caticha, A. & Caticha-Ellis, S. (1982). *Phys. Rev. B*, **25**, 971–983.
- Chang, S. L., Stetsko, Y. P., Tang, M. T., Lee, Y. R., Sun, W. H., Yabashi, M. & Ishikawa, T. (2005). *Phys. Rev. Lett.* **94**, 174801.

- DuMond, J. W. M. (1937). *Phys. Rev.* **52**, 872–883.
- Fister, T. T., Seidler, G. T., Wharton, L., Battle, A. R., Ellis, T. B., Cross, J. O., Macrander, A. T., Elam, W. T., Tyson, T. A. & Qian, Q. (2006). *Rev. Sci. Instrum.* **77**, 063901.
- Gog, T., Casa, D. M., Knopp, J., Kim, J., Upton, M. H., Krakora, R., Jaski, A., Said, A., Yavaş, H., Gretarsson, H. & Huang, X. R. (2018). *J. Synchrotron Rad.* **25**, 1030–1035.
- Graeff, W. & Materlik, G. (1982). *Nucl. Instrum. Methods Phys. Res.* **195**, 97–103.
- Hashizume, H. & Nakahata, T. (1988). *Jpn. J. Appl. Phys.* **27**, L1568–L1571.
- Hill, J. P., Coburn, D. S., Kim, Y.-J., Gog, T., Casa, D. M., Kodituwakku, C. N. & Sinn, H. (2007). *J. Synchrotron Rad.* **14**, 361–365.
- Hönnicke, M. G., Bianco, L. M., Ceppi, S. A., Cusatis, C., Huang, X., Cai, Y. Q. & Stutz, G. E. (2016). *J. Appl. Cryst.* **49**, 1443–1453.
- Hönnicke, M. G., Conley, R., Cusatis, C., Kakuno, E. M., Zhou, J., Bouet, N., Marques, J. B. & Vicentin, F. C. (2014). *J. Appl. Cryst.* **47**, 1658–1665.
- Hönnicke, M. G. & Cusatis, C. (2009). *J. Appl. Cryst.* **42**, 999–1003.
- Hönnicke, M. G., Huang, X., Cusatis, C., Kodituwakku, C. N. & Cai, Y. Q. (2013). *J. Appl. Cryst.* **46**, 939–944.
- Hönnicke, M. G., Kakuno, E. M., Kellerman, G., Mazzaro, I., Abler, D. & Cusatis, C. (2008). *Opt. Express*, **16**, 9284–9289.
- Huang, X.-R. (2011). *J. Synchrotron Rad.* **18**, 899–906.
- Huang, X.-R., Gog, T., Kim, J., Kasman, E., Said, A. H., Casa, D. M., Wiczorek, M., Hönnicke, M. G. & Assoufid, L. (2018). *J. Appl. Cryst.* **51**, 140–147.
- Huang, X. R., Siddons, D. P., Macrander, A. T., Peng, R. W. & Wu, X. S. (2012). *Phys. Rev. Lett.* **108**, 224801.
- Huotari, S., Pylkkänen, T., Verbeni, R., Monaco, G. & Hämäläinen, K. (2011). *Nat. Mater.* **10**, 489–493.
- Ishikawa, D., Ellis, D. S., Uchiyama, H. & Baron, A. Q. R. (2015). *J. Synchrotron Rad.* **22**, 3–9.
- Ketenoglu, D., Harder, M., Klementiev, K., Upton, M., Taherkhani, M., Spiwek, M., Dill, F.-U., Wille, H.-C. & Yavaş, H. (2015). *J. Synchrotron Rad.* **22**, 961–967.
- Kim, J., Casa, D., Said, A., Krakora, R., Kim, B. J., Kasman, E., Huang, X. & Gog, T. (2018). *Sci. Rep.* **8**, 1958.
- Kohra, K. & Matsushita, T. (1972). *Z. Naturforsch.* **27**, 484–487.
- Macrander, A., Pereira, N., Stoeckl, C., Huang, X. & Kasman, E. (2019). *J. Appl. Cryst.* **52**, 115–121.
- Mortensen, D. R., Seidler, G. T., Bradley, J. A., Lipp, M. J., Evans, W. J., Chow, P., Xiao, Y.-M., Boman, G. & Bowden, M. E. (2013). *Rev. Sci. Instrum.* **84**, 083908.
- Sahle, C. J., Rosa, A. D., Rossi, M., Cerantola, V., Spiekermann, G., Petitgirard, S., Jacobs, J., Huotari, S., Moretti Sala, M. & Mirone, A. (2017). *J. Synchrotron Rad.* **24**, 269–275.
- Said, A. H., Gog, T., Wiczorek, M., Huang, X., Casa, D., Kasman, E., Divan, R. & Kim, J. H. (2018). *J. Synchrotron Rad.* **25**, 373–377.
- Sanchez del Rio, M., Perez-Bocanegra, N., Shi, X., Honkimäki, V. & Zhang, L. (2015). *J. Appl. Cryst.* **48**, 477–491.
- Schülke, W. & Nagasawa, H. (1984). *Nucl. Instrum. Methods Phys. Res.* **222**, 203–206.
- Sergueev, I., Wille, H.-C., Hermann, R. P., Bessas, D., Shvyd'ko, Y. V., Zajac, M. & Rüffer, R. (2011). *J. Synchrotron Rad.* **18**, 802–810.
- Shvyd'ko, Y. V., Lerche, M., Kuetsgens, U., Rüter, H. D., Alatas, A. & Zhao, J. (2006). *Phys. Rev. Lett.* **97**, 235502.
- Shvyd'ko, Y. V., Lerche, M., Wille, H. C., Gerdau, E., Lucht, M., Rüter, H. D., Alp, E. E. & Khachatryan, R. (2003). *Phys. Rev. Lett.* **90**, 013904.
- Sokaras, D., Weng, T.-C., Nordlund, D., Alonso-Mori, R., Velikov, P., Wenger, D., Garachtchenko, A., George, M., Borzenets, V., Johnson, B., Rabedeau, T. & Bergmann, U. (2013). *Rev. Sci. Instrum.* **84**, 053102.
- Sutter, J. P., Baron, A. Q. R., Ishikawa, T. & Yamazaki, H. (2005). *J. Phys. Chem. Solids*, **66**, 2306–2309.
- Sutter, J. P., Baron, A. Q. R., Miwa, D., Nishino, Y., Tamasaku, K. & Ishikawa, T. (2006). *J. Synchrotron Rad.* **13**, 278–280.
- Sykora, B. & Peisl, J. (1970). *Z. Angew. Math. Phys.* **30**, 320.
- Tirao, G., Stutz, G. & Cusatis, C. (2004). *J. Synchrotron Rad.* **11**, 335–342.
- Verbeni, R., Pylkkänen, T., Huotari, S., Simonelli, L., Vankó, G., Martel, K., Henriquet, C. & Monaco, G. (2009). *J. Synchrotron Rad.* **16**, 469–476.
- Yavaş, H., Sutter, J. P., Gog, T., Wille, H.-C. & Baron, A. Q. R. (2017). *MRS Bull.* **42**, 424–429.